

Classification and Spectral Evolution of Outbursts of Aql X–1

C. Güngör¹, T. Güver², & K. Y. Eksi¹

¹*Istanbul Technical University, Faculty of Science and Letters, Physics Engineering Department, 34469, Istanbul, Turkey*

²*Istanbul University, Science Faculty, Department of Astronomy and Space Sciences, Beyazıt, 34119, Istanbul, Turkey*

ABSTRACT

We present a broad classification of all outbursts detected with the All-Sky Monitor (ASM) on the Rossi X-Ray Timing Explorer (RXTE) and the Monitor of All Sky X-Ray Image (MAXI) of Aql X–1. We identify three types of outbursts; *long-high*, *medium-low*, and *short-low*, based on the duration and maximum flux. We analyse the trends in the “phase-space” of flux-derivative versus flux to demonstrate the differences in the three identified outburst types. We present a spectral analysis of the observations of Aql X–1 performed by the Proportional Counter Array (PCA) onboard RXTE during the 2000 and 2011 outbursts of the long-high class and the 2010 outburst of the medium-low class. We model the source spectrum with a hybrid thermal/non-thermal hot plasma emission model (EQPAIR in XSPEC, Coppi 2000) together with a Gaussian component to model the Fe K α emission line. We construct time histories of the source flux, the optical depth of the corona (τ), the seed photon temperature (kT_{bb}) and the hard state compactness (l_{h}) for these three outbursts. We show that the physical parameters of either classes reach the same values throughout the outbursts, the only difference being the maximum flux. We discuss our results in the terms of modes of interaction of the star with the disc and size of the disc kept hot by irradiation. We conclude that irradiation is the dominant physical process leading to the different classes of outbursts.

Key words: X-rays: binaries X-rays:individual Aql X–1

1 INTRODUCTION

Aql X–1 is a low mass X-ray binary in which a neutron star accretes matter from an accretion disc which is supplied by the Roche lobe filling low mass companion. Aql X–1 is also classified as a soft X-ray transient (SXTs, see Campana et al. 1998, for a review) system; most of the time it is in a quiescent state with a luminosity of $L_X \approx 10^{33} \text{ erg s}^{-1}$ (Verbunt et al. 1994) while occasionally it exhibits outbursts which at the peak can reach to $L_X \approx 10^{37} \text{ erg s}^{-1}$ resulting from the enhanced accretion rate, \dot{M} , in the disc. According to the disc instability model (DIM; see Lasota 2001, for a review) the viscous-thermal instability in the disc (van Paradijs 1996) is the cause of the enhanced accretion.

As with all transient systems, the X-ray morphology of outbursts of Aql X–1 show a wide range of lightcurve patterns. A typical lightcurve pattern is described as a fast-rise-exponential-decay (FRED; Chen et al. 1997). A FRED lightcurve can be reproduced with the DIM only if the irradiation of the outer parts of the disc by the X-rays from the central source is taken into account (King & Ritter 1998).

Apart from events that show FRED like behavior and its varieties there is also a low intensity state (LIS; Wachter et al. 2002) in which the optical and near IR emission flux is above quiescence but the lightcurve does not follow the FRED trend and can last longer. What leads to such distinct outburst lightcurves is not very well understood.

A clue to the diversity of the outburst lightcurve morphology could be the variety of spectral states the transient systems exhibit. An SXT in the rising phase of the outburst would usually enter the high/soft (HS) state from the low/hard (LH) state and return to the LH state during the decay of the outburst (see Remillard & McClintock 2006, for a review of spectral states in black hole systems). Spectral states of SXTs in which the accreting objects are neutron stars are similar to those in black hole systems. This similarity is not well understood given that the neutron stars have hard surfaces where the energy of the accreting matter would be thermalized whereas the black holes have event horizons through which the energy could be advected with the accretion flow. Aql X–1 is classified as an atoll source (van der Klis 1994; Hasinger & van der Klis 1989) according to the tracks it follows on the X-ray color-color

and hardness-intensity diagrams, and spectral variations it shows. In this case HS and LH states roughly correspond to banana and island states (Hasinger & van der Klis 1989), respectively.

The HS state is associated with a standard geometrically thin optically thick Keplerian disc (Shakura & Sunyaev 1973) while the LH state is associated with a geometrically thick optically thin advection dominated disc (Ichimaru 1977; Narayan & Yi 1994) and a corona at which the soft seed photons from the disc blackbody are up-scattered by relativistic electrons. In order to address the low luminosity in the hard state it is also necessary to introduce the truncation of the inner region of the geometrically thin accretion disk.

The different modes of interaction between the magnetosphere of the neutron star and the surrounding disc, that take place at different accretion rates, which changes by three orders of magnitude during an outburst, may also have a role in the diversity of the lightcurve morphology. During the decay phase in which the mass flux is decreasing, the inner radius of the disk moves outwards. Once the inner radius is pushed beyond the corotation radius, $R_c = (GM/\Omega^2)^{1/3}$, at which Keplerian angular velocity in the disk equals the angular velocity of the magnetosphere Ω , it is expected that accretion onto the star is inhibited by the centrifugal barrier and the system is said to be in the “propeller” stage (Illarionov & Sunyaev 1975; Davies et al. 1979; Davies & Pringle 1981; Wang & Robertson 1985). Aql X-1 showed a rapid decay of luminosity accompanied by an abrupt spectral transition during the decline of its 1997 outburst which was interpreted as the onset of the “propeller” stage (Campana et al. 1998; Zhang et al. 1998).

Aql X-1 is one of the most active SXTs making it possibly the most suitable system for classifying outbursts, investigating the interplay between irradiation, transition to propeller stage and spectral transitions. In §2, we present a broad classification of outbursts based on the durations and the maximum fluxes. In §3, we explain the details of observation and analyzing procedure, and provide the results of observational analysis. In §4, we discuss the evolution of the physical parameters which we obtained and we associate them with the outburst types we classified. Finally, in §5 we present our conclusion.

2 CLASSIFICATION OF OUTBURSTS OF AQL X-1

We present a broad classification of the outbursts of Aql X-1 based on the duration and the maximum flux. A different classification for the outbursts of this object was recently presented by Asai et al. (2013) based on the spectral transitions (see also Maitra & Bailyn 2008; Campana et al. 2013). The classification we present may not be an alternative to this as will be discussed in §4.2. In Figure 1 (upper panel), we show all outbursts as observed by ASM (Levine et al. 1996) aboard the RXTE (Jahoda et al. 1996); the 2011 and the 2013 outbursts observed by MAXI (Matsuoka et al. 2009). For each instrument we used the daily average values in the 2–10 keV and 2–20 keV range, respectively. We calibrated the data sets from the two instruments by comparing the peak count rate of the 2009 and

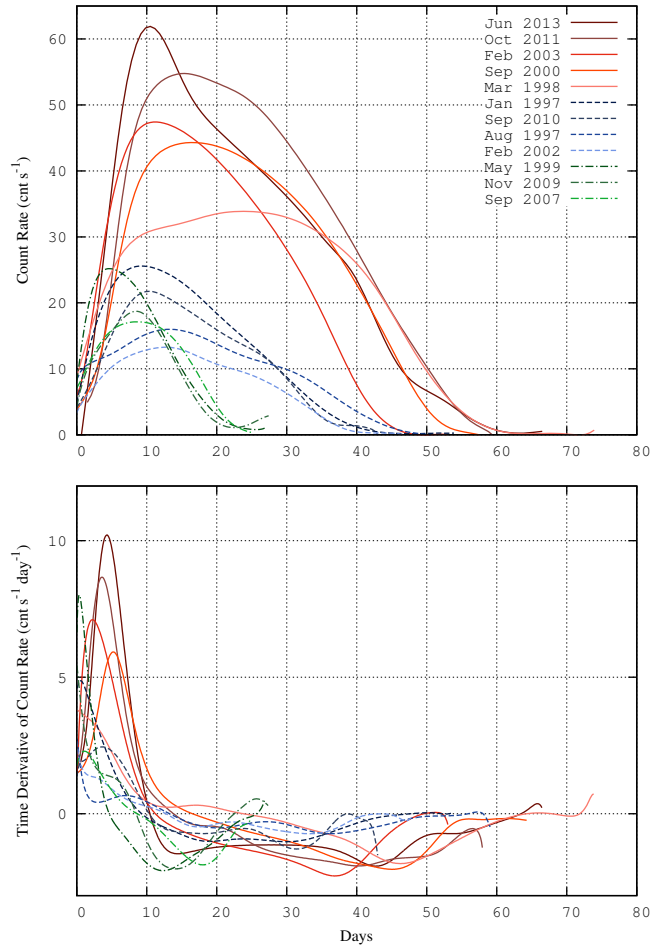


Figure 1. ASM and MAXI lightcurves of outbursts (upper panel) and their time derivative. The data is smoothed with Bézier process for visualization. Three types of outbursts can be discriminated: (i) The long-high outbursts shown with solid lines (red). These events last about 50-60 days and reach a count rate of 37-61 cnt/s. (ii) The medium-low outbursts, shown with dashed lines (blue), last about 40-50 days and reach a count rate of 13-25 cnt/s. (iii) The short-low outbursts, shown with dashed-dot lines (green), last about 20 days and reach a count rate of 17-25 cnt/s.

2010 outbursts, which were observed by both detectors. Using the near-simultaneous detections, we determined a conversion factor of ≈ 22 . The beginning of the outbursts were determined as the point at which the count-rate reaches 5 cnt/s. To see the trends in the lightcurves more clearly we have smoothed the data sets using the Bézier spline method.

The upper panel of Figure 1 shows the evolution of count-rate in all data sets. It is clearly seen that 2013 outburst is the brightest outburst of Aql X-1 in the data set, as was suggested by Güver et al. (2013). It is also seen that there are three types of outbursts. The *long-high* outbursts have long duration with 50-60 days and are luminous, reaching a maximum flux of 37-61 cnt/s. The *medium-low* outbursts last for 40-50 days, reaching a maximum flux of 13-25 cnt/s. The *short-low* outbursts last for approximately 20 days reaching a maximum flux of 17-25 cnt/s. Note that this classification does not include outbursts corresponding to LIS that last even longer than the long-high outbursts at a LH state, but never reaches to count-rate of 5 cnt/s

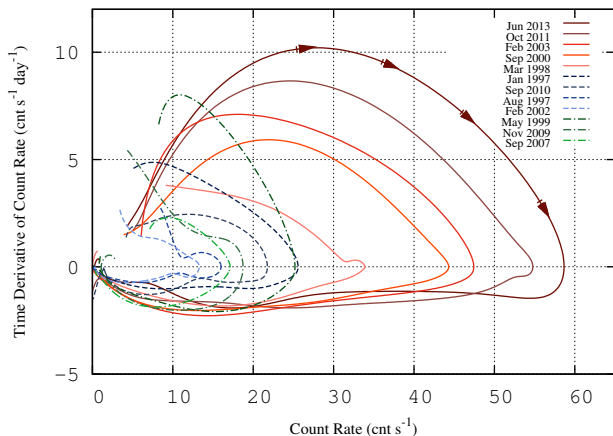


Figure 2. The outbursts in the counts/s versus counts/s/day “phase space”. The arrows on the curve of June 2013 event shows the direction of time. Outbursts start from the upper-left domain, move clockwise, pass from the $y = 0$ at the peak of the outbursts, and reach to the lower-left domain (quiescence).

level, which is our criterion to calibrate initial times of all outbursts.

Conversion of the data sets to continuous curves by Bézier spline method allows us to evaluate the time derivative of the flux curves, which we show in the lower panel of Figure 1. We see that the rising stages of the bright outbursts consist of two sub-stages in which the flux change rate increases and then decreases. The medium-low outbursts show a more complex trend. It is also seen that the decay stage also roughly consists of two sub-stages in which the flux decay rate first speeds-up and then slows down. The behavior at the lowest flux levels are much more complicated, showing variability at a time-scale of days.

Figure 2 shows the evolution of the outbursts in the “phase space” of flux-rate versus flux. An outburst starts from the upper-left domain of the plot, moves clockwise as shown with arrows on the outermost curve for the June 2013 and ends near the origin.

3 OBSERVATION AND DATA ANALYSIS

In order to better characterize the distinction between different types of outbursts we used the monitoring observations performed by RXTE/PCA. We analysed the 2000, 2010, and 2011 outbursts of Aql X-1. Based on the above mentioned classification, the 2000 and 2011 outbursts are members of the long-high class and the 2010 outburst is a member of the medium-low class.

The times of RXTE observations during 2010 and 2011 outbursts are shown on the MAXI lightcurve in Figure 3. It is clearly visible that the 2011 outburst is much more luminous than 2010 outburst and the RXTE pointings in 2011 covers the outburst completely, including both the rise and decay phases. We also focused on the 2000 outburst as a comparison, since it is one of the most luminous outbursts with detailed RXTE observations.

As Aql X-1 is a bright source, using one of the four PCUs is sufficient to produce high S/N spectrum. We used PCU2, which has been calibrated the best and has been

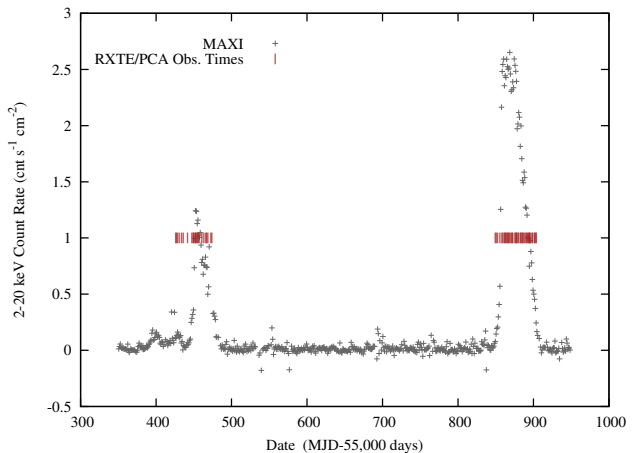


Figure 3. The long-term evolution of Aql X-1 as observed by MAXI between June 2010 to January 2012. Dates of RXTE/PCA observations are marked with vertical bars.

continuously working. We analysed the data using HEASOFT v6.11 and created response matrices separately for each data set using the PCARSP version 11.7. We created the background spectra using the latest module file for bright sources, *pcabkgd_cmbrightvle_eMv20051128.mdl*.

We used XSPEC v12.7.0 for the spectral analysis. After subtracting the background from the original data, we fit 3–30 keV energy range, retaining the band at which the PCA detector is the most sensitive. We added a systematic error of 1%. During the 2010 and 2011 outbursts, we determined 2 and 4 Type-I thermonuclear X-ray bursts, respectively. We ignored the events detected 100 seconds before the start and 100 seconds after the end of these bursts. Following Maccarone & Coppi (2003b) we fitted the spectrum with the EQPAIR model (Coppi 2000), which is a hybrid comptonization model bridging the purely Maxwellian and purely power-law particle energy distributions, responsible for the emission, in a self-consistent way. EQPAIR uses the ratio of relative heating and cooling of electrons on account of radiative processes and Coulomb interactions for solving the electron distribution. Many other models have been employed in the literature for fitting the X-ray spectra of LMXBs (see also Raichur et al. 2011; Maitra & Bailyn 2004). Statistically, all these models fit the X-ray spectra as successfully as EQPAIR. EQPAIR has been used for fitting X-ray spectra of disc flows with corona in LMXBs with black hole components (Caballero-Garcia et al. 2008). As such EQPAIR can not address how much the neutron star contributes to the thermal and non-thermal emission from these sources. Our choice of EQPAIR for modeling the spectra is motivated by the purpose of investigating the role of the parameters of the corona in the irradiation of the outer disc. Using EQPAIR also allows us to compare our results with earlier studies (Maccarone & Coppi 2003b). Since EQPAIR is a hybrid model for both plasma, it is able to fit all the energy range between 3.0 keV and 30.0 keV, with the addition of a statistically necessary Gaussian component.

We fixed the neutral hydrogen column density at $N_H = 3.4 \times 10^{21} \text{ cm}^{-2}$ (Maccarone & Coppi 2003b). The soft photon compactness (l_{bb}) and the fraction of power supplied to energetic particles which goes into accelerating

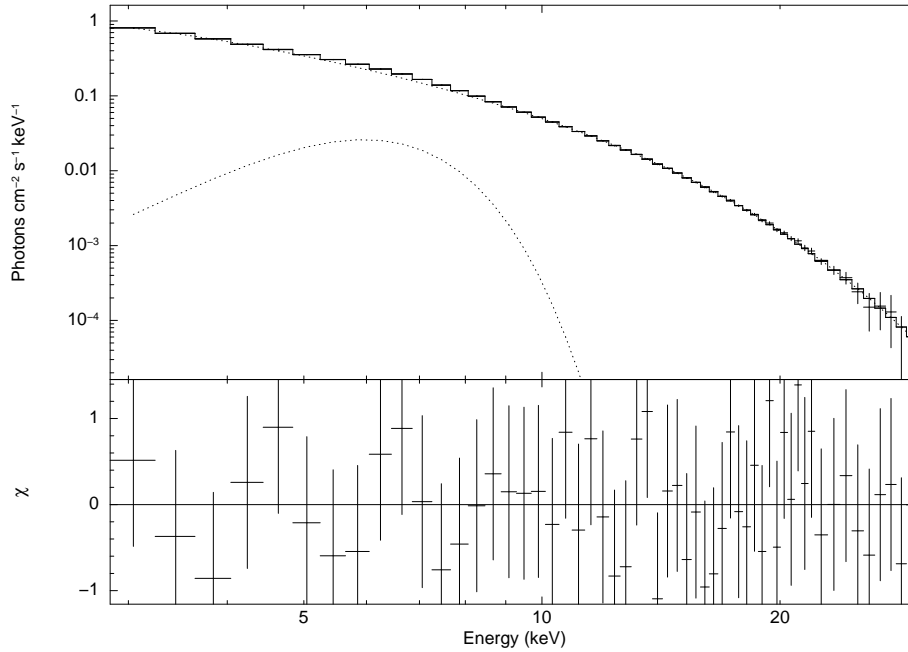


Figure 4. Upper panel shows the X-ray spectrum (Obs ID 96440-01-03-04) and the best fit model between 3.0 keV and 30.0 keV together with the best fit EQPAIR model and a Gaussian line. Lower panel shows the residuals in terms of sigma.

non-thermal particles (l_{nt}/l_h) were frozen at 1.0 and 0.0, respectively. This allows us to determine l_h in terms of l_{bb} . Welsh et al. (2000) shows that the orbital inclination should be greater than 36 degree. The inclination angle was chosen as 60 degrees for simplicity. All the other parameters of EQPAIR model, were set to default values and kept frozen during the fit (following Maccarone & Coppi 2003b). After we reached the best fit parameters of EQPAIR model with minimum χ^2 , we added a Gaussian component to take into account the systematic residuals due to the iron line between 5.8 keV and 7.0 keV for each observation. In Figure 4, we show an example X-ray spectrum of Aql X-1 obtained during the peak of the 2011 outburst (Obs ID 96440-01-03-04) and the best fit EQPAIR model with a Gaussian line.

For all the X-ray spectra of Aql X-1 obtained by RXTE/PCA observations, we followed the procedure described above. Overall, for the 2000 outburst we have 55 pointings, when the source was in the outburst phase. The 2010 outburst was covered with 24 pointings. Seven of these observations were obtained when the source was still in quiescent phase, which allows us to better characterize how parameters evolve as the source advances from quiescence to outburst. During the 2011 outburst, we have 43 data sets that completely cover both, the rise and decay phases.

The free parameters of EQPAIR model are the optical depth of the corona (τ), the seed photon temperature ($k_B T_{bb}$) and the hard state compactness (l_h). Figure 5 shows the time evolution of these parameters during 2000, 2010 and 2011 outbursts. The spectral parameters evolve in a very similar way in each outburst: (i) The optical depth of the corona increases during the rise and becomes stable until the end of the decay. (ii) The hard state compactness decreases to ≈ 0.5 immediately after the onset of outbursts. (iii) We see that the seed photon temperature slightly decreases as the outbursts proceed. We note however that this

is the least constrained parameter in our model because the inferred values are too low for the RXTE/PCA sensitivity range, during the outburst. The best fit parameters of EQPAIR model and Gaussian component including the errors are shown in Table 1, Table 2 and Table 3.

4 DISCUSSION

We consider three different causes for the diversity of outburst morphology presented in §2: (i) A longer waiting time before an outburst might lead to larger amount of matter accumulation in the disc resulting in long-high type outbursts; (ii) it might be that only during the *long-high* outbursts the inner radius of the disc penetrates the corotation radius leading to substantial accretion while the *medium-low* and the *short-low* both proceed by partial accretion during the spin-down regime; (iii) a different portion of the disc is involved in different types of outbursts probably because of different irradiation geometries involved. In the following we discuss these three options in detail and discuss the implications of the results of our spectral analysis.

4.1 Is the quiescent stage duration related to the different outburst classes?

One naturally expects that a longer waiting time between two outbursts might lead to a larger amount of matter accumulation in the disc resulting with a more luminous outburst. This possibility was considered by Campana et al. (2013) (see their fig. 6) who checked whether the peak flux of outbursts are correlated with the preceding waiting times before the outbursts. They found only a very weak correlation indicating that the duration of the quiescent stage is

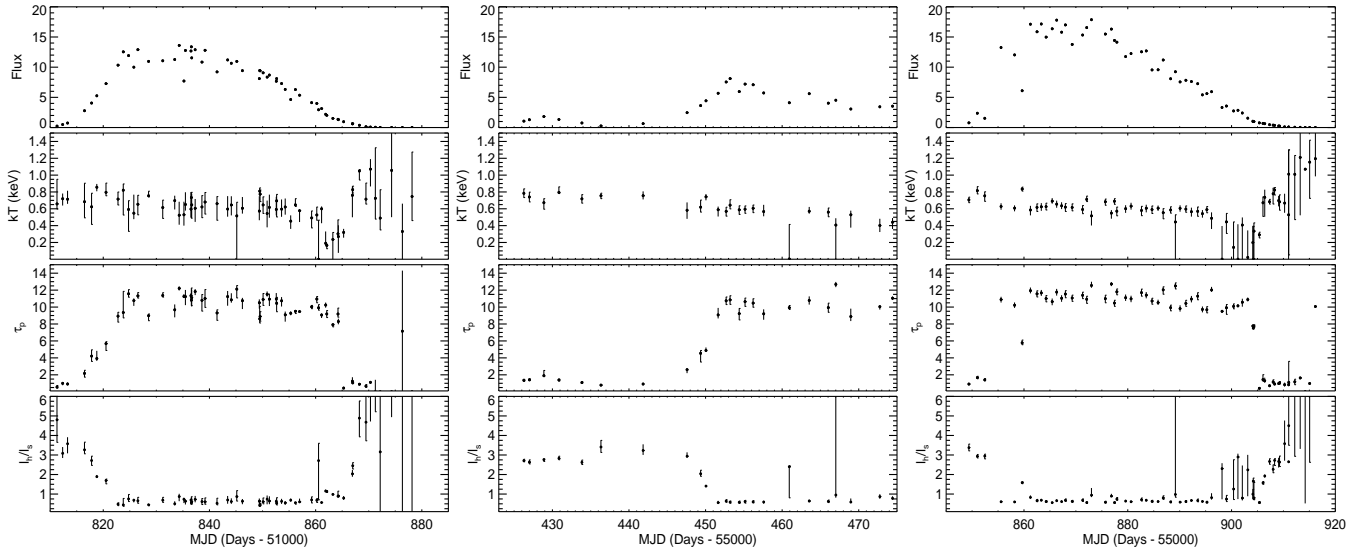


Figure 5. Spectral evolution of Aql X-1 during the 2000 (left panel), 2010 (middle panel) and 2011 (right panel) outbursts. From upper to lower, panels show the evolution of unabsorbed total flux, temperature of the seed photons, optical depth, and the ratio of hard to soft compactness, respectively. All fluxes are given in units of 10^{-9} erg s $^{-1}$ cm $^{-2}$.

not the main cause of the difference between the long-high, medium-low and short-low classes.

4.2 Transition to the propeller stage as the cause of the rapid decay stage

The rapid decay of luminosity during the decline of the 1997 outburst of Aql X-1 was interpreted as the onset of the “propeller” stage (Campana et al. 1998; Zhang et al. 1998). A similar rapid decline stage is shown also by the first discovered AMXP (Wijnands & van der Klis 1998) SAX J1808.4–3658 in several of its outbursts. This was associated with transition to propeller stage by Gilfanov et al. (1998). The 1997 outburst of Aql X-1 which led to the propeller interpretation is of the low-medium class. It can be seen from Figure 1 that, compared to the 1997 event, the 1998 outburst shows a much more prominent transition from slow decay to rapid decay at a count-rate level of ≈ 27 . Assuming that this flux level corresponds to the critical mass flow rate that places the inner radius on the corotation radius, one is forced to conclude that the system remains in the spin-down stage throughout the medium-low and short-low outbursts, accreting only a fraction of the inflowing mass because the maximum count-rate for these outbursts remain below ≈ 27 . Within this scenario the inner radius can penetrate the corotation radius only for the brightest outbursts, which possibly could address why many outbursts are stunted and why pulsations are elusive.

In the case of SAX J1808.4–3658 (but not Aql X-1) the X-ray pulsations continue to be detected even in the rapid decay stage (Psaltis & Chakrabarty 1999). In order to address this issue Rappaport et al. (2004) argued that it is not energetically possible for the magnetosphere to eject matter from the system as the magnetosphere expands to the corotation radius with the decaying mass flux. They presented disk solutions in which the inner radius of the disk remains on the corotation radius for a large range of mass flux such that accretion and X-ray pulsations continue.

Ibragimov & Poutanen (2009) concluded from the variations of the pulse profiles that the size of the hot spot on the neutron star changes throughout the outburst which then indicates that the inner radius of the disc does recede during the decay of the outburst. Ekşi & Kutlu (2011) associated the rapid decay stage of SAX J1808.4–3658 with a partial accretion regime (Menou et al. 1999; Ustyugova et al. 2006a; Romanova et al. 2004) in which matter at the disc mid-plane is centrifugally inhibited while matter vertically away from the mid-plane can accrete. This requires the inner region of the disc to be geometrically thick as required by radiatively inefficient disc models that address the LH state.

The onset of a propeller during an outburst may affect the number of thermonuclear X-ray bursts occurring during an outburst. To test the propeller scenario, we therefore investigated the observed Type-I X-ray bursts during different outbursts. Using the X-ray burst catalogue of Galloway et al. (2008) we identified the number of X-ray bursts detected during a given outburst. Although such an analysis is subject to selection effects due to the varying coverage of the RXTE/PCA of individual outbursts, we found that a similar number of X-ray bursts and photospheric radius expansion events have been observed from different types of outbursts. For example, during the short-low outburst observed in 1999, two photospheric radius expansion events were observed together with one Type-I burst. On the other hand during the 2000 outburst, which is a long-high event according to our classification, 4 Type-I X-ray bursts were observed of which one is a photospheric radius expansion event. A similar trend is also observed during the two outbursts observed in 1997 and 2002, which are all medium-low type outbursts. During these outbursts 1, 4, and 5 type-I X-ray bursts have been observed with one photospheric radius expansion events during each of the 1997 outbursts and 2 during the 2002 outburst. We note however that there are exceptions, for example the short-low outburst that occurred in 1998 was observed with RXTE/PCA with 24 pointings. Despite the dense coverage not a single X-ray burst was ob-

served during the outburst from the source. This seems to support the argument discussed above that there had been a transition to the propeller stage during the 1998 outburst.

Recently, [Asai et al. \(2013\)](#) suggested transition to the propeller stage as an explanation for the rapid decay in the lightcurves of 4U 1608–52, Aql X–1 and XTE J1701–462 discriminating transition to propeller stage from the spectral transitions by using luminosity dwell-time distributions (see also [Matsuoka & Asai 2013](#)). This does not mean that irradiation is not present in the system, but only that it may not be the cause of the rapid decay stage. Presence of jets ([Tudose et al. 2009](#)) in this system associated with transition from HS to LH state may also indicate the role of the “propeller” for ejecting matter from the system (see e.g. [Romanova et al. \(2009\)](#); [Lii et al. \(2012\)](#); [Ustyugova et al. \(2006b\)](#); [Lovelace et al. \(1999\)](#)).

A well known argument against the propeller interpretation is that not only neutron star SXTs but some black hole SXTs also show a “brink” in the decay stages of their outbursts implying a common origin for the rapid decay (e.g. [Jonker et al. 2004](#)). As black holes do not have a magnetosphere, propeller mechanism can not be at work in these systems and thus can not be the common cause for the rapid decay stage. The presence of similar spectral transitions also suggests a common mechanism disfavouring transition to propeller as the cause of the spectral transitions.

Yet another argument against the propeller interpretation is the hysteresis effect: [Maccarone & Coppi \(2003a\)](#) showed that the LH to HS spectral transition at the initial rise of the burst occurs at a luminosity 5 times greater than that of the transition from HS to LH at the declining stage suggesting that propeller mechanism alone can not be the driver of the spectral transitions as one would expect transitions between accretion and propeller stages to be at a single luminosity for a certain system ([Davidson & Ostriker 1973](#)). More recently, [Yu & Dolence \(2007\)](#) discovered, during the declining stage of the very faint 2001 outburst of Aql X–1, a spectral transition from LH to HS state suggesting that mass flow rate, \dot{M} , is not the sole parameter determining the luminosity of the transition and mentioned the role of change in the mass flux.

These problems with the propeller interpretation can partly be surpassed by suggesting that the transition to propeller stage is not the cause of the spectral transition but a consequence of it. If the inner disc makes a transition to a geometrically thick radiatively inefficient flow causing the transition to the LH state, the mass flux and ram pressure suddenly drops as the flow becomes sub-keplerian; the magnetosphere pushes the disc outwards which may then cause the system to transit to the propeller stage if the disc is pushed beyond the corotation radius.

4.3 Irradiation as the parameter inducing different outburst durations and peak fluxes

The difficulties in interpreting the rapid decline as transition to the propeller stage led to the favored view that the cause of transition to the rapid decay stage is related to the outer disc disconnecting from the inner disc by entering the cool low-viscosity state as this region is no longer irradiated ([Powell et al. 2007](#)), the third possibility we would like to discuss.

Recently, [Campana et al. \(2013\)](#) presented an in-depth analysis of the outbursts observed from Aql X–1 using the irradiated disc model of [Powell et al. \(2007\)](#) and fitted the observed lightcurves. This brings in two different estimates of the outer radius of the disc: either via the viscous timescale at the outer radius or via the furthest point that is irradiated in the disc. One naturally expects that the peak flux would be proportional to the size of the disc kept hot by irradiation. In Figure 6, we present the estimated outer disc radius versus the peak count-rate we identify in §2. The outer radius values are taken from [Campana et al. \(2013\)](#) who estimated them based on the irradiation model ([Powell et al. 2007](#)). We obtained corresponding peak fluxes from the smoothed outbursts in §2. We find that the peak flux is roughly correlated with the disk size. As the maximum size of the disc is determined by the Roche lobe radius, only during the long-high type outbursts the disc can have radii reaching that range while the disc during the medium-low and the short-low outbursts either does not fill the Roche lobe radius, or that the outer parts of such a disc is not sufficiently hot to be active and is not involved in the outburst. If the latter is the case then the correlation of the peak flux with the disc size is consistent with the view that larger portion of the disc is involved in the long-high type of outbursts probably due to the different irradiation efficiency of the outer parts.

Although the number of data for each individual type of outburst is small, it is possible to infer from Figure 6 that the long-high and the medium-low outbursts have different slopes while the short-low outbursts show a large scatter and does not reveal its trend. The smaller slope of the long-high outbursts implies that for such large sized discs a slight increase in the disc size leads to much higher peak flux. This is because the amount of matter and angular momentum within a ring of definite width increase rapidly with radial distance from the center. Thus a small change in the irradiation geometry may lead to a small change in the heated outer radius which then would lead to drastic changes in the outburst morphology.

4.4 Implications of spectral analysis

We have considered the possibility that the difference between the three outburst types of the classification in §2 could originate from different spectral properties the disc displays. In order to check this possibility we have analyzed the spectral evolution during the 2000, 2010 and 2011 outbursts which are of the long-high type (2000 and 2011) and medium-low type (2010). With this analysis our aim is to better characterize these events and to better understand their differences. Using the EQPAIR model ([Coppi 2000](#)), we followed the evolution of the optical depth in the non-thermal Comptonizing corona, the seed photon temperature and the hard state compactness parameters. Our results show that independent of the duration and the maximum flux of an outburst, the spectral parameters follow a well defined and reproducible track during the long-high and medium-low type outbursts that are analysed here. A typical example of a short-low type outburst is the May 1999 outburst. This outburst was also monitored with the RXTE/PCA and the X-ray spectra was modeled with the EQPAIR model by [Maccarone & Coppi \(2003b\)](#). Compar-

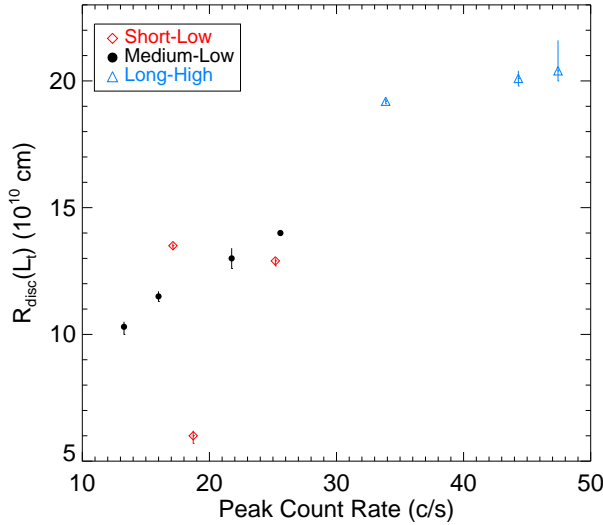


Figure 6. Outer disc radius versus the peak count-rate of outbursts of Aql X-1. The outer radii of the outbursts are estimated by Campana et al. (2013) via the furthest point irradiated in the disc. We see a linear correlation as would be expected that a larger outburst would require a larger portion of the disk to be involved in the outburst. Different classes of outbursts are shown with different symbols. The long-high and the medium-low outbursts have a tighter correlation with a different slope while short-low class shows no correlation.

ing the spectral evolution during this outburst with the results presented here, we see that the optical depth and the compactness parameters evolve in a very similar way. The only difference in the deduced spectral parameters is a slight increase in the seed photon temperature measured at the beginning of the 1999 outburst (see Figure 1. of Maccarone & Coppi 2003b), which longer outbursts in our sample do not show.

In Figure 7, we show the evolution of the optical depth with flux. Once an outburst commences, together and almost simultaneously with the flux, the scattering optical depth of the corona increases. During the increase the Spearman's rank correlation coefficient between the two parameters is 0.92. This correlation persists till the optical depth reaches a saturation point, which is between 9 to 12 and independent from the peak flux of the outburst. The optical depth remains at the saturation values even during the decline of the outburst and drops to the pre-outburst values with a substantial time delay.

We have also investigated the relation between the compactness parameter l_h/l_s and the optical depth of the corona as shown in Figure 8. The bottom right corner of the figure corresponds to the HS state and upper left corner stands for the LH state. For $1 < \tau < 10$ the relation is inverse and linear. This less populated region corresponds to the transitions between these two spectral states. As seen in Figure 5, l_h/l_s shows similar time delay as τ does, which is reflected in the linear relation seen in Figure 8

The time evolution of the flux of the Gaussian line at ≈ 6.5 keV follows a well defined and reproducible trend similar to the flux obtained from the EQPAIR model. In Figure 9 we show the line flux as a function of the continuum flux. The relation between the flux of the Fe line and the continuum

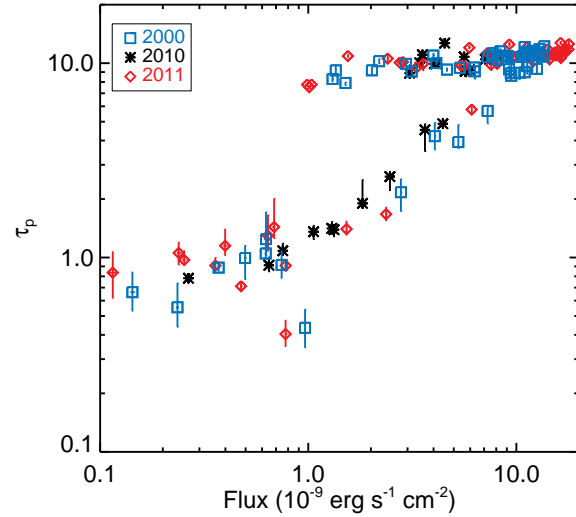


Figure 7. Evolution of the scattering optical depth of the corona as a function of unabsorbed source flux. During the outbursts the parameters start from the lower left corner, proceed to the upper right corner during the enhancement stage, remain on the upper horizontal branch during the decay of the outburst and finally drop to the pre-outburst values.

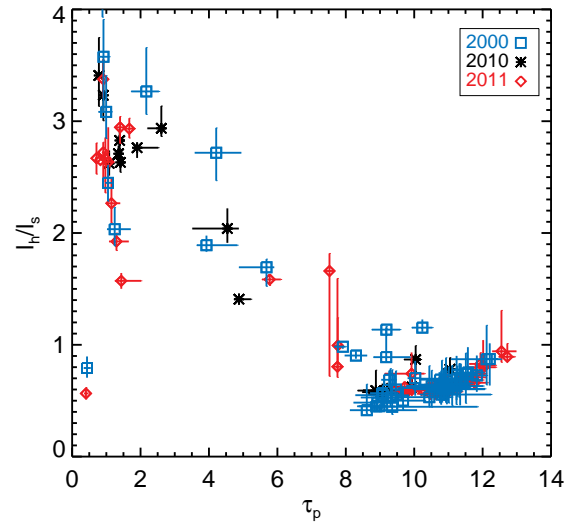


Figure 8. The relation between the compactness parameter l_h/l_s and the optical depth of the corona. We have eliminated data with very large errorbars ($\Delta(l_h/l_s) > 1$).

flux does not seem to be exactly linear at low fluxes ($< 6 \times 10^{-9} \text{ erg cm}^{-2} \text{ s}^{-1}$). As the flux increases, however, the correlation becomes more linear.

Apart from some exceptions our X-ray spectral analysis and observations of Type-I X-ray bursts indicate that the peak flux and duration of a given outburst is relatively independent of the region in the X-ray binary that determines the shape of the X-ray spectra. The only difference between the various classes of outbursts seems to be the emitting radius of the seed photons which determines the total observed X-ray flux.

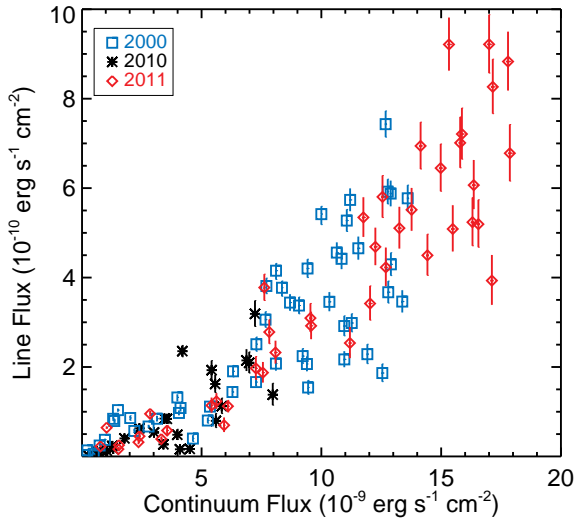


Figure 9. Variation of unabsorbed flux of the Gaussian iron line component as a with the EQPAIR model flux.

5 CONCLUSION

We have presented a broad classification of the outbursts of Aql X-1 based on the duration and maximum flux. We identified three types of outbursts, *long-high*, *medium-low* and *short-low*. In terms of total energy released, the *long-high* outbursts overwhelms the others.

We analysed the spectral evolution throughout three outbursts of Aql X-1 observed by RXTE, the 2000, 2010 and 2011, using the EQPAIR model. The 2010 outburst is a member of the medium-low type while 2000 and 2011 outbursts are members of the long-high type. These outbursts, together with the 1999 outburst analyzed by Maccarone & Coppi (2003b) which is of the short-low type, give us an opportunity to discuss three types of outbursts analysed with the same method. Our spectral analysis showed that all of the inferred parameters evolve in a very similar way regardless of the different classes of the outbursts, with only difference being the maximum flux. This implies that the ingredient in the X-ray binary that shapes the observed X-ray spectra is not the cause of the different outburst types.

Irradiation of the disc modulates the disc size involved in the outbursts thereby leading to different luminosities in different classes. We showed a correlation between the maximum flux and the outer radius of the disc inferred by Campana et al. (2013) which demonstrates the role of irradiation as the main cause for the different peak luminosities. We argued that the transition to the propeller or partial accretion regime induced by transition to a geometrically thick disc might contribute to the diversity in the observed lightcurve morphology.

ACKNOWLEDGEMENTS

This work is supported by The Scientific and Technological Council of TURKEY (TUBITAK) with the project number 112T105. We thank M. Ali Alpar and Ersin Göğüş for their valuable comments and careful reading of the manuscript. TG acknowledges support from Bilim Akademisi - The Sci-

ence Academy, Turkey under the BAGEP program. KYE thanks Ralph Neuhauser and Klaus Werner for hospitality during his visit to Jena and Tübingen, respectively.

REFERENCES

- Asai K., Matsuoka M., Mihara T., Sugizaki M., Serino M., Nakahira S., Negoro H., Ueda Y., Yamaoka K., 2013, *ApJ*, 773, 117
- Caballero-Garcia M. D., Miller J. M., Fabian A. C., 2008, in *Proceedings of the 7th INTEGRAL Workshop The high-energy emission from GX 339-4 as seen with INTEGRAL and XMM-Newton*
- Campana S., Colpi M., Mereghetti S., Stella L., Tavani M., 1998, *A&ARv*, 8, 279
- Campana S., Coti Zelati F., D’Avanzo P., 2013, *MNRAS*, 432, 1695
- Campana S., Stella L., Mereghetti S., Colpi M., Tavani M., Ricci D., Fiume D. D., Belloni T., 1998, *ApJ*, 499, L65
- Chen W., Shrader C. R., Livio M., 1997, *ApJ*, 491, 312
- Coppi P. S., 2000, in *AAS/High Energy Astrophysics Division #5 Vol. 32 of Bulletin of the American Astronomical Society, EQPAIR: A Hybrid Thermal/Non-Thermal Model for the Spectra of X-Ray Binaries*. p. 1217
- Davidson K., Ostriker J. P., 1973, *ApJ*, 179, 585
- Davies R. E., Fabian A. C., Pringle J. E., 1979, *MNRAS*, 186, 779
- Davies R. E., Pringle J. E., 1981, *MNRAS*, 196, 209
- Ekşi K. Y., Kutlu E., 2011, in Göğüş E., Belloni T., Ertan Ü., eds, *American Institute of Physics Conference Series Vol. 1379 of American Institute of Physics Conference Series, Accretion in the spin-down regime*. pp 156–159
- Galloway D. K., Muno M. P., Hartman J. M., Psaltis D., Chakrabarty D., 2008, *ApJS*, 179, 360
- Gilfanov M., Revnivtsev M., Sunyaev R., Churazov E., 1998, *A&A*, 338, L83
- Güver T., Ak T., Güngör C., Ekşi Y., 2013, *The Astronomer’s Telegram*, 5129, 1
- Hasinger G., van der Klis M., 1989, *A&A*, 225, 79
- Ibragimov A., Poutanen J., 2009, *MNRAS*, 400, 492
- Ichimaru S., 1977, *ApJ*, 214, 840
- Illarionov A. F., Sunyaev R. A., 1975, *A&A*, 39, 185
- Jahoda K., Swank J. H., Giles A. B., Stark M. J., Strohmayer T., Zhang W., Morgan E. H., 1996, in *Siegmund O. H., Gummin M. A., eds, Society of Photo-Optical Instrumentation Engineers (SPIE) Conference Series Vol. 2808 of Society of Photo-Optical Instrumentation Engineers (SPIE) Conference Series, In-orbit performance and calibration of the Rossi X-ray Timing Explorer (RXTE) Proportional Counter Array (PCA)*. pp 59–70
- Jonker P. G., Gallo E., Dhawan V., Rupen M., Fender R. P., Dubus G., 2004, *MNRAS*, 351, 1359
- King A. R., Ritter H., 1998, *MNRAS*, 293, L42
- Lasota J.-P., 2001, *New Astronomy Reviews*, 45, 449
- Levine A. M., Bradt H., Cui W., Jernigan J. G., Morgan E. H., Remillard R., Shirey R. E., Smith D. A., 1996, *ApJ*, 469, L33
- Lii P., Romanova M., Lovelace R., 2012, *MNRAS*, 420, 2020
- Lovelace R. V. E., Romanova M. M., Bisnovatyi-Kogan G. S., 1999, *ApJ*, 514, 368
- Maccarone T. J., Coppi P. S., 2003a, *MNRAS*, 338, 189

- Maccarone T. J., Coppi P. S., 2003b, *A&A*, 399, 1151
- Maitra D., Bailyn C. D., 2004, *ApJ*, 608, 444
- Maitra D., Bailyn C. D., 2008, *ApJ*, 688, 537
- Matsuoka M., Asai K., 2013, *PASJ*, 65, 26
- Matsuoka M., Kawasaki K., Ueno S., Tomida H., Kohama M., Suzuki M., Adachi Y., Ishikawa M., Mihara T., Sugizaki M., Isobe N., Nakagawa Y., 2009, *PASJ*, 61, 999
- Menou K., Esin A. A., Narayan R., Garcia M. R., Lasota J.-P., McClintock J. E., 1999, *ApJ*, 520, 276
- Narayan R., Yi I., 1994, *ApJ*, 428, L13
- Powell C. R., Haswell C. A., Falanga M., 2007, *MNRAS*, 374, 466
- Psaltis D., Chakrabarty D., 1999, *ApJ*, 521, 332
- Raichur H., Misra R., Dewangan G., 2011, *MNRAS*, 416, 637
- Rappaport S. A., Fregeau J. M., Spruit H., 2004, *ApJ*, 606, 436
- Remillard R. A., McClintock J. E., 2006, *ARA&A*, 44, 49
- Romanova M. M., Ustyugova G. V., Koldoba A. V., Lovelace R. V. E., 2004, *ApJ*, 616, L151
- Romanova M. M., Ustyugova G. V., Koldoba A. V., Lovelace R. V. E., 2009, *MNRAS*, 399, 1802
- Shakura N. I., Sunyaev R. A., 1973, *A&A*, 24, 337
- Tudose V., Fender R. P., Linares M., Maitra D., van der Klis M., 2009, *MNRAS*, 400, 2111
- Ustyugova G. V., Koldoba A. V., Romanova M. M., Lovelace R. V. E., 2006a, *ApJ*, 646, 304
- Ustyugova G. V., Koldoba A. V., Romanova M. M., Lovelace R. V. E., 2006b, *ApJ*, 646, 304
- van der Klis M., 1994, *ApJS*, 92, 511
- van Paradijs J., 1996, *ApJ*, 464, L139
- Verbunt F., Belloni T., Johnston H. M., van der Klis M., Lewin W. H. G., 1994, *A&A*, 285, 903
- Wachter S., Hoard D. W., Bailyn C. D., Corbel S., Kaaret P., 2002, *ApJ*, 568, 901
- Wang Y.-M., Robertson J. A., 1985, *A&A*, 151, 361
- Welsh W. F., Robinson E. L., Young P., 2000, *AJ*, 120, 943
- Wijnands R., van der Klis M., 1998, *Nature*, 394, 344
- Yu W., Dolence J., 2007, *ApJ*, 667, 1043
- Zhang S. N., Yu W., Zhang W., 1998, *ApJ*, 494, L71

Table 1. Best fit parameters of EQPAIR model and the Gaussian line for 2000 outburst.

JD-51000 (days)	t_h/l_s	kT_{bb} (eV)	τ_p	$\chi^2/\text{d.o.f.}$	Line Energy (keV)	Line Width (keV)	Flux ^a _{eqpair}	Flux ^b _{gauss}
811.2856	4.80 ^{+1.27} _{-1.15}	658 ⁺²⁹² ₋₆₁	0.55 ^{+0.18} _{-0.12}	0.65	5.80 ^{+0.33} _{-5.80}	1.71 ^c _{-0.36}	0.235 ^{+0.004} _{-0.004}	0.136 ^{+0.008} _{-0.008}
812.3495	3.08 ^{+0.32} _{-0.24}	719 ⁺⁶² ₋₈₀	0.99 ^{+0.16} _{-0.22}	0.68	6.34 ^{+0.19} _{-0.21}	0.57 ^{+0.33} _{-0.29}	0.497 ^{+0.004} _{-0.004}	0.061 ^{+0.008} _{-0.008}
813.2773	3.58 ^{+0.33} _{-0.49}	714 ⁺¹⁰¹ ₋₅₅	0.92 ^{+0.17} _{-0.14}	0.82	5.80 ^{+0.24} _{-5.80}	1.40 ^{+0.18} _{-0.27}	0.745 ^{+0.004} _{-0.004}	0.245 ^{+0.013} _{-0.015}
816.4667	3.27 ^{+0.39} _{-0.21}	684 ⁺²²⁰ ₋₁₉₂	2.17 ^{+0.37} _{-0.44}	0.68	6.07 ^{+0.17} _{-0.19}	1.20 ^{+0.20} _{-0.18}	2.787 ^{+0.008} _{-0.007}	0.670 ^{+0.038} _{-0.037}
817.7979	2.72 ^{+0.22} _{-0.25}	624 ⁺¹⁶¹ ₋₂₀₉	4.21 ^{+0.63} _{-0.74}	0.67	6.04 ^{+0.17} _{-0.19}	1.20 ^{+0.19} _{-0.17}	4.055 ^{+0.011} _{-0.011}	0.973 ^{+0.054} _{-0.054}
818.7868	1.89 ^{+0.09} _{-0.06}	856 ⁺³⁹ ₋₄₇	3.93 ^{+0.90} _{-0.28}	0.54	6.52 ^{+0.14} _{-0.16}	0.85 ^{+0.20} _{-0.18}	5.260 ^{+0.011} _{-0.012}	0.804 ^{+0.061} _{-0.059}
820.5169	1.69 ^{+0.07} _{-0.17}	795 ⁺¹¹⁰ ₋₄₁	5.68 ^{+0.23} _{-0.81}	0.54	6.38 ^{+0.14} _{-0.16}	1.13 ^{+0.17} _{-0.15}	7.273 ^{+0.009} _{-0.026}	1.663 ^{+0.091} _{-0.089}
822.7745	0.48 ^{+0.07} _{-0.08}	715 ⁺⁸⁴ ₋₇₀	8.92 ^{+0.46} _{-0.70}	0.56	6.29 ^{+0.24} _{-0.30}	1.34 ^{+0.24} _{-0.21}	10.334 ^{+0.026} _{-0.026}	3.457 ^{+0.218} _{-0.211}
823.7689	0.45 ^{+0.33} _{-0.07}	820 ⁺⁷⁵ ₋₂₉₅	9.36 ^{+2.49} _{-0.63}	0.69	6.72 ^{+0.20} _{-0.24}	0.82 ^{+0.30} _{-0.25}	10.958 ^{+0.030} _{-0.033}	1.865 ^{+0.203} _{-0.193}
824.7611	0.75 ^{+0.23} _{-0.13}	592 ⁺¹⁰⁴ ₋₂₆₀	11.57 ^{+0.49} _{-0.40}	0.32	6.26 ^{+0.22} _{-0.26}	0.91 ^{+0.26} _{-0.23}	11.919 ^{+0.038} _{-0.035}	2.287 ^{+0.223} _{-0.213}
825.7550	0.69 ^{+0.03} _{-0.11}	547 ⁺²²¹ ₋₇₀	10.76 ^{+0.26} _{-0.62}	0.64	5.81 ^{+0.21} _{-0.24}	1.42 ^{+0.08} _{-0.17}	10.000 ^{+0.029} _{-0.015}	5.418 ^{+0.175} _{-0.235}
826.5129	0.65 ^{+0.18} _{-0.13}	653 ⁺¹⁰⁷ ₋₁₂₅	11.32 ^{+0.39} _{-0.26}	0.39	6.25 ^{+0.18} _{-0.21}	1.15 ^{+0.18} _{-0.22}	12.902 ^{+0.034} _{-0.034}	4.296 ^{+0.260} _{-0.252}
828.5344	0.45 ^{+0.01} _{-0.05}	755 ⁺⁵⁴ ₋₁₃	8.98 ^{+0.20} _{-0.59}	0.68	6.61 ^{+0.18} _{-0.20}	0.93 ^{+0.17} _{-0.20}	10.958 ^{+0.030} _{-0.029}	2.171 ^{+0.184} _{-0.175}
831.2024	0.69 ^{+0.14} _{-0.11}	615 ⁺⁸⁸ ₋₁₂₉	11.37 ^{+0.32} _{-0.19}	0.53	5.96 ^{+0.20} _{-0.19}	1.38 ^{+0.17} _{-0.16}	11.061 ^{+0.028} _{-0.032}	5.274 ^{+0.250} _{-0.244}
833.4586	0.50 ^{+0.13} _{-0.08}	697 ⁺⁵⁸ ₋₁₀₅	9.67 ^{+0.64} _{-0.89}	0.74	6.52 ^{+0.17} _{-0.20}	0.97 ^{+0.19} _{-0.17}	11.268 ^{+0.033} _{-0.031}	2.984 ^{+0.207} _{-0.198}
834.3003	0.87 ^{+0.14} _{-0.24}	523 ⁺¹⁶⁰ ₋₁₁₂	12.21 ^{+0.24} _{-0.25}	0.35	5.92 ^{+0.15} _{-0.16}	1.33 ^{+0.15} _{-0.16}	13.604 ^{+0.033} _{-0.036}	5.772 ^{+0.295} _{-0.289}
835.1903	0.73 ^{+0.08} _{-0.19}	529 ⁺¹⁵⁴ ₋₁₂₉	11.26 ^{+0.27} _{-0.19}	0.43	5.88 ^{+0.18} _{-0.19}	1.29 ^{+0.12} _{-0.15}	7.705 ^{+0.022} _{-0.023}	3.812 ^{+0.176} _{-0.172}
835.4761	0.63 ^{+0.10} _{-0.17}	651 ⁺⁷⁸ ₋₇₃	11.24 ^{+0.10} _{-0.01}	0.34	6.06 ^{+0.17} _{-0.22}	1.37 ^{+0.17} _{-0.15}	12.771 ^{+0.034} _{-0.035}	5.920 ^{+0.280} _{-0.274}
836.5150	0.70 ^{+0.03} _{-0.24}	596 ⁺²⁰³ ₋₁₀₀	11.34 ^{+0.28} _{-0.37}	0.52	5.88 ^{+0.19} _{-0.19}	1.48 ^{+0.12} _{-0.15}	12.683 ^{+0.035} _{-0.036}	7.430 ^{+0.295} _{-0.290}
836.5906	0.56 ^{+0.31} _{-0.07}	734 ⁺⁶¹ ₋₂₄₅	10.81 ^{+1.44} _{-0.64}	0.64	6.47 ^{+0.19} _{-0.22}	1.03 ^{+0.22} _{-0.19}	13.376 ^{+0.036} _{-0.036}	3.463 ^{+0.254} _{-0.244}
836.6590	0.61 ^{+0.21} _{-0.15}	647 ⁺¹³³ ₋₁₅₃	11.11 ^{+0.96} _{-0.03}	0.42	6.05 ^{+0.21} _{-0.24}	1.25 ^{+0.20} _{-0.18}	11.543 ^{+0.034} _{-0.033}	4.655 ^{+0.261} _{-0.255}
837.3107	0.73 ^{+0.18} _{-0.15}	605 ⁺¹¹¹ ₋₁₆₁	11.83 ^{+0.29} _{-0.42}	0.62	5.95 ^{+0.23} _{-0.18}	1.46 ^{+0.17} _{-0.18}	12.892 ^{+0.035} _{-0.034}	5.877 ^{+0.291} _{-0.285}
838.5825	0.61 ^{+0.15} _{-0.15}	622 ⁺¹³⁵ ₋₁₂₇	10.79 ^{+0.69} _{-1.27}	0.78	6.11 ^{+0.18} _{-0.21}	1.19 ^{+0.18} _{-0.16}	10.843 ^{+0.031} _{-0.031}	4.419 ^{+0.238} _{-0.231}
839.1655	0.60 ^{+0.20} _{-0.12}	680 ⁺¹¹³ ₋₁₄₃	11.01 ^{+1.05} _{-0.05}	0.44	6.34 ^{+0.18} _{-0.21}	1.05 ^{+0.20} _{-0.18}	12.792 ^{+0.034} _{-0.033}	3.672 ^{+0.251} _{-0.242}
841.4233	0.53 ^{+0.26} _{-0.08}	661 ⁺⁸⁴ ₋₁₉₇	9.31 ^{+0.36} _{-0.87}	0.65	6.48 ^{+0.18} _{-0.22}	0.97 ^{+0.21} _{-0.19}	9.220 ^{+0.027} _{-0.026}	2.244 ^{+0.169} _{-0.162}
843.4235	0.70 ^{+0.20} _{-0.19}	597 ⁺¹⁵⁴ ₋₉₀	11.24 ^{+0.66} _{-1.08}	0.50	5.93 ^{+0.21} _{-0.19}	1.45 ^{+0.15} _{-0.17}	11.201 ^{+0.030} _{-0.034}	5.737 ^{+0.258} _{-0.253}
844.1205	0.62 ^{+0.16} _{-0.12}	646 ⁺¹⁰³ ₋₁₂₄	10.85 ^{+0.34} _{-0.34}	0.44	6.13 ^{+0.17} _{-0.22}	1.32 ^{+0.17} _{-0.16}	10.645 ^{+0.031} _{-0.027}	4.558 ^{+0.223} _{-0.223}
845.1457	0.87 ^{+0.30} _{-0.23}	516 ⁺¹⁶² ₋₅₁₆	12.12 ^{+0.42} _{-1.04}	0.25	6.06 ^{+0.24} _{-0.06}	1.12 ^{+0.23} _{-0.21}	10.955 ^{+0.033} _{-0.029}	2.916 ^{+0.227} _{-0.219}
846.2087	0.63 ^{+0.12} _{-0.15}	606 ⁺¹³⁴ ₋₆₃	10.75 ^{+0.33} _{-0.99}	0.45	6.08 ^{+0.17} _{-0.22}	1.28 ^{+0.17} _{-0.16}	9.423 ^{+0.027} _{-0.030}	4.203 ^{+0.208} _{-0.203}
849.3941	0.63 ^{+0.14} _{-0.19}	573 ⁺¹⁷⁷ ₋₁₀₉	10.51 ^{+0.40} _{-0.70}	0.48	5.82 ^{+0.25} _{-0.82}	1.45 ^{+0.11} _{-0.20}	8.108 ^{+0.025} _{-0.025}	4.153 ^{+0.163} _{-0.197}
849.4632	0.42 ^{+0.23} _{-0.03}	810 ⁺³⁸ ₋₄₄	8.61 ^{+1.47} _{-0.26}	0.77	6.71 ^{+0.21} _{-0.24}	0.90 ^{+0.29} _{-0.24}	9.447 ^{+0.029} _{-0.025}	1.542 ^{+0.160} _{-0.151}
849.5347	0.45 ^{+0.07} _{-0.04}	774 ⁺⁴⁹ ₋₈₈	8.89 ^{+0.56} _{-0.55}	0.83	6.60 ^{+0.21} _{-0.26}	1.03 ^{+0.25} _{-0.21}	9.398 ^{+0.023} _{-0.025}	2.068 ^{+0.172} _{-0.164}
850.1023	0.61 ^{+0.19} _{-0.11}	646 ⁺⁹⁵ ₋₁₀₁	10.89 ^{+0.70} _{-0.70}	0.41	6.20 ^{+0.19} _{-0.22}	1.21 ^{+0.18} _{-0.16}	9.067 ^{+0.025} _{-0.025}	3.374 ^{+0.190} _{-0.185}
850.8640	0.74 ^{+0.19} _{-0.26}	544 ⁺¹⁵³ ₋₁₆₅	11.51 ^{+0.33} _{-0.26}	0.72	5.81 ^{+0.24} _{-0.18}	1.44 ^{+0.10} _{-0.18}	8.355 ^{+0.025} _{-0.023}	3.772 ^{+0.151} _{-0.190}
851.2877	0.64 ^{+0.24} _{-0.16}	617 ⁺¹⁵¹ ₋₁₂₂	10.93 ^{+0.66} _{-0.81}	0.60	6.09 ^{+0.21} _{-0.25}	1.32 ^{+0.19} _{-0.17}	8.692 ^{+0.025} _{-0.023}	3.440 ^{+0.188} _{-0.183}
852.5877	0.63 ^{+0.09} _{-0.16}	592 ⁺¹⁵⁰ ₋₇₀	10.96 ^{+0.70} _{-0.47}	1.10	6.01 ^{+0.23} _{-0.01}	1.30 ^{+0.21} _{-0.19}	7.669 ^{+0.023} _{-0.023}	3.059 ^{+0.176} _{-0.172}
852.6531	0.53 ^{+0.28} _{-0.09}	694 ⁺⁷⁷ ₋₁₉₁	10.44 ^{+0.70} _{-1.00}	0.72	6.47 ^{+0.21} _{-0.27}	1.02 ^{+0.26} _{-0.22}	8.104 ^{+0.024} _{-0.024}	2.077 ^{+0.167} _{-0.159}
853.5833	0.63 ^{+0.13} _{-0.13}	596 ⁺¹¹⁵ ₋₉₁	10.74 ^{+0.44} _{-0.68}	0.54	6.11 ^{+0.22} _{-0.26}	1.22 ^{+0.22} _{-0.20}	7.288 ^{+0.022} _{-0.022}	2.510 ^{+0.161} _{-0.156}
854.2723	0.55 ^{+0.09} _{-0.10}	621 ⁺¹⁰¹ ₋₉₁	9.09 ^{+0.38} _{-0.81}	0.43	6.22 ^{+0.25} _{-0.31}	1.28 ^{+0.24} _{-0.21}	6.314 ^{+0.019} _{-0.017}	1.904 ^{+0.132} _{-0.126}
855.3036	0.69 ^{+0.08} _{-0.07}	454 ⁺⁹² ₋₉₂	9.27 ^{+0.22} _{-0.23}	0.51	6.61 ^{+0.42} _{-0.42}	0.68 ^{+0.35} _{-0.35}	4.639 ^{+0.012} _{-0.011}	0.400 ^{+0.073} _{-0.066}
856.1874	0.56 ^{+0.02} _{-0.07}	647 ⁺⁷³ ₋₁₉	9.50 ^{+0.07} _{-0.26}	0.49	6.48 ^{+0.22} _{-0.28}	1.08 ^{+0.26} _{-0.22}	6.289 ^{+0.018} _{-0.017}	1.441 ^{+0.118} _{-0.112}
856.9696	0.60 ^{+0.17} _{-0.01}	577 ⁺¹⁵ ₋₁₃₄	9.47 ^{+0.18} _{-0.04}	0.52	6.40 ^{+0.25} _{-0.30}	1.05 ^{+0.26} _{-0.23}	5.350 ^{+0.016} _{-0.016}	1.114 ^{+0.100} _{-0.095}
859.2409	0.70 ^{+0.15} _{-0.16}	492 ⁺⁸² ₋₁₁₉	10.03 ^{+0.17} _{-0.22}	0.62	6.26 ^{+0.23} _{-0.29}	1.14 ^{+0.24} _{-0.21}	4.122 ^{+0.013} _{-0.012}	1.084 ^{+0.083} _{-0.079}
860.2152	0.68 ^{+0.08} _{-0.11}	527 ⁺⁹⁴ ₋₆₂	10.95 ^{+0.30} _{-0.44}	0.51	5.80 ^{+0.32} _{-0.27}	1.41 ^{+0.15} _{-0.12}	3.989 ^{+0.012} _{-0.012}	1.319 ^{+0.071} _{-0.087}
860.5474	2.71 ^c _{-2.01}	1 ⁺⁴⁶⁴ ₋₁	9.92 ^{+0.37} _{-0.28}	0.73	6.46 ^{+0.31} _{-0.42}	1.10 ^{+0.37} _{-0.29}	2.948 ^{+0.015} _{-0.019}	0.494 ^{+0.108} _{-0.096}
861.1194	0.57 ^{+0.03} _{-0.06}	600 ⁺²⁸ ₋₁₇₁	9.06 ^{+0.18} _{-0.71}	0.67	6.39 ^{+0.31} _{-0.45}	1.39 ^{+0.36} _{-0.35}	3.139 ^{+0.013} _{-0.006}	0.844 ^{+0.065} _{-0.062}
861.8861	1.15 ^{+0.07} _{-0.04}	190 ⁺¹⁴⁰ ₋₂₆	10.24 ^{+0.29} _{-0.31}	0.72	6.20 ^c _{-0.17}	1.49 ^{+0.17} _{-0.17}	2.192 ^{+0.007} _{-0.008}	0.570 ^{+0.048} _{-0.045}
862.0931	1.14 ^{+0.03} _{-0.05}	164 ⁺¹⁴ ₋₃₉	9.19 ^{+0.40} _{-0.42}	0.82	5.95 ^{+0.45} _{-0.73}	1.73 ^{+0.47} _{-0.34}	2.022 ^{+0.010} _{-0.005}	0.860 ^{+0.050} _{-0.048}
863.2400	0.98 ^{+0.01} _{-0.02}	236 ⁺⁸³ ₋₂₃₆	7.91 ^{+0.25} _{-0.25}	0.67	5.88 ^{+0.88} _{-5.88}	1.69 ^{+0.34} _{-0.17}	1.509 ^{+0.004} _{-0.005}	1.036 ^{+0.036} _{-0.035}
864.2082	0.89 ^{+0.26} _{-0.04}	303 ⁺¹⁶⁵ ₋₃₄	9.18 ^{+0.70} _{-0.37}	0.55	5.84 ^{+0.44} _{-0.84}	1.74 ^c _{-0.35}	1.356 ^{+0.006} _{-0.006}	0.793 ^{+0.037} _{-0.040}
864.2775	0.90 ^{+0.04} _{-0.03}	270 ⁺¹³⁴ ₋₁₉₄	8.30 ^{+0.33} _{-0.33}	0.64	5.99 ^{+0.37} _{-0.99}	1.64 ^c _{-0.31}	1.308 ^{+0.003} _{-0.007}	0.841 ^{+0.041} _{-0.040}
865.2722	0.79 ^{+0.10} _{-0.09}	320 ⁺⁴² ₋₆₃	0.43 ^{+0.11} _{-0.09}	0.95	5.88 ^{+0.21} _{-0.24}	1.13 ^{+0.23} _{-0.24}	0.965 ^{+0.005} _{-0.006}	0.373 ^{+0.025} _{-0.024}
866.9225	2.03 ^{+0.20} _{-0.15}	760 ⁺¹⁰⁷ ₋₂₆₁	1.24 ^{+0.47} _{-0.22}	1.02	6.08 ^{+0.28} _{-0.29}	0.62 ^{+0.13} _{-0.00}	0.627 ^{+0.013} _{-0.012}	0.049 ^{+0.024} _{-0.019}
866.9779	2.45 ^{+0.16} _{-0.16}	827 ⁺⁴² ₋₄₀	1.05 ^{+0.11} _{-0.07}	2.21	5.60 ^c _{-0.07}	0.93 ^c _{-0.07}	0.625 ^{+0.006} _{-0.007}	0.065 ^c _{-0.007}
868.2361	4.89 ^{+0.88} _{-0.96}	1049 ⁺¹⁶ ₋₁₀₇	0.89 ^{+0.04} _{-0.04}	0.72	5.87 ^c _{-0.25}	0.25 ^c _{-0.25}	0.371 ^{+0.002} _{-0.002}	0.000 ^{+0.011} _{-0.000}
869.4744	4.68 ^{+1.81} _{-0.95}	714 ⁺¹⁹¹ ₋₅₈	0.66 ^{+0.18} _{-0.14}	0.62				

Table 2. Same as Table 1 but for 2010 outburst.

JD-55000 (days)	l_h/l_s	kT_{bb} (eV)	τ_p	$\chi^2/\text{d.o.f.}$	Line Energy (keV)	Line Width (keV)	Flux $^a_{eqpair}$	Flux $^b_{gauss}$
426.2689	2.71 $^{+0.07}_{-0.06}$	784 $^{+53}_{-50}$	1.36 $^{+0.12}_{-0.11}$	2.12	5.60 $^{+0.11}_{-0.10}$	1.01 $^{+0.22}_{-0.21}$	1.048 $^{+0.006}_{-0.007}$	0.127 $^{+0.025}_{-0.024}$
426.9906	2.63 $^{+0.12}_{-0.09}$	740 $^{+57}_{-58}$	1.41 $^{+0.10}_{-0.12}$	1.14	5.60 $^{+0.10}_{-0.24}$	1.24 $^{+0.20}_{-0.19}$	1.275 $^{+0.009}_{-0.008}$	0.235 $^{+0.031}_{-0.031}$
428.8847	2.76 $^{+0.04}_{-0.09}$	672 $^{+47}_{-77}$	1.90 $^{+0.11}_{-0.62}$	1.92	5.60 $^{+0.09}_{-0.60}$	1.23 $^{+0.14}_{-0.14}$	1.782 $^{+0.006}_{-0.006}$	0.403 $^{+0.022}_{-0.031}$
430.8469	2.83 $^{+0.11}_{-0.07}$	795 $^{+66}_{-14}$	1.39 $^{+0.12}_{-0.10}$	2.06	5.60 $^{+0.07}_{-0.60}$	0.97 $^{+0.20}_{-0.19}$	1.313 $^{+0.004}_{-0.019}$	0.169 $^{+0.029}_{-0.029}$
433.8503	2.62 $^{+0.12}_{-0.11}$	718 $^{+50}_{-51}$	1.08 $^{+0.05}_{-0.10}$	1.59	5.60 $^{+0.13}_{-0.60}$	0.94 $^{+0.25}_{-0.25}$	0.746 $^{+0.006}_{-0.007}$	0.089 $^{+0.019}_{-0.020}$
436.3373	3.41 $^{+0.34}_{-0.28}$	755 $^{+30}_{-34}$	0.78 $^{+0.04}_{-0.04}$	0.82	6.68 $^{+0.25}_{-0.24}$	0.25 $^{+0.42}_{-0.25}$	0.264 $^{+0.004}_{-0.004}$	0.022 $^{+0.005}_{-0.005}$
441.8428	3.23 $^{+0.31}_{-0.23}$	756 $^{+51}_{-44}$	0.91 $^{+0.07}_{-0.09}$	0.68	6.02 $^{+0.27}_{-0.35}$	0.76 $^{+0.51}_{-0.45}$	0.636 $^{+0.010}_{-0.010}$	0.110 $^{+0.026}_{-0.025}$
447.5829	2.94 $^{+0.20}_{-0.10}$	582 $^{+93}_{-102}$	2.61 $^{+0.41}_{-0.11}$	0.80	5.60 $^{+0.16}_{-0.60}$	1.35 $^{+0.14}_{-0.17}$	2.405 $^{+0.006}_{-0.007}$	0.629 $^{+0.031}_{-0.032}$
449.3527	2.04 $^{+0.18}_{-0.13}$	619 $^{+84}_{-58}$	4.54 $^{+1.03}_{-0.34}$	0.83	6.21 $^{+0.17}_{-0.19}$	1.08 $^{+0.23}_{-0.20}$	3.552 $^{+0.019}_{-0.011}$	0.841 $^{+0.091}_{-0.088}$
450.0526	1.41 $^{+0.05}_{-0.05}$	742 $^{+33}_{-41}$	4.88 $^{+0.14}_{-0.35}$	1.10	5.88 $^{+0.17}_{-0.19}$	1.62 $^{+1.62}_{-0.17}$	4.197 $^{+0.021}_{-0.020}$	2.355 $^{+0.128}_{-0.126}$
451.6399	0.56 $^{+0.09}_{-0.04}$	589 $^{+37}_{-80}$	9.07 $^{+0.41}_{-0.83}$	0.50	6.54 $^{+0.23}_{-0.29}$	0.78 $^{+0.30}_{-0.25}$	5.596 $^{+0.031}_{-0.032}$	0.796 $^{+0.167}_{-0.151}$
452.6867	0.64 $^{+0.07}_{-0.06}$	570 $^{+49}_{-57}$	10.74 $^{+0.45}_{-0.45}$	0.72	5.87 $^{+0.30}_{-0.87}$	1.49 $^{+0.25}_{-0.24}$	7.229 $^{+0.036}_{-0.035}$	3.189 $^{+0.294}_{-0.283}$
453.1981	0.59 $^{+0.05}_{-0.05}$	643 $^{+64}_{-44}$	10.85 $^{+0.53}_{-0.49}$	0.58	6.38 $^{+0.22}_{-0.28}$	0.82 $^{+0.29}_{-0.25}$	7.970 $^{+0.038}_{-0.038}$	1.381 $^{+0.256}_{-0.233}$
454.3926	0.58 $^{+0.06}_{-0.05}$	588 $^{+48}_{-54}$	9.23 $^{+0.74}_{-0.61}$	0.79	6.50 $^{+0.20}_{-0.26}$	0.87 $^{+0.28}_{-0.24}$	5.844 $^{+0.026}_{-0.032}$	1.125 $^{+0.181}_{-0.166}$
455.1530	0.62 $^{+0.06}_{-0.08}$	595 $^{+39}_{-48}$	10.64 $^{+0.56}_{-0.42}$	0.73	6.27 $^{+0.20}_{-0.25}$	1.08 $^{+0.23}_{-0.20}$	6.988 $^{+0.033}_{-0.033}$	2.094 $^{+0.243}_{-0.228}$
456.2053	0.60 $^{+0.06}_{-0.05}$	606 $^{+39}_{-52}$	10.47 $^{+0.49}_{-0.51}$	0.53	6.30 $^{+0.24}_{-0.31}$	1.19 $^{+0.26}_{-0.22}$	6.873 $^{+0.033}_{-0.034}$	2.147 $^{+0.252}_{-0.237}$
457.5870	0.59 $^{+0.06}_{-0.08}$	567 $^{+80}_{-56}$	9.20 $^{+0.70}_{-0.53}$	0.66	6.22 $^{+0.28}_{-0.37}$	1.25 $^{+0.29}_{-0.25}$	5.568 $^{+0.028}_{-0.028}$	1.621 $^{+0.204}_{-0.191}$
460.9298	2.40 $^{+0.04}_{-1.59}$	4 $^{+411}_{-4}$	9.93 $^{+0.20}_{-0.26}$	0.46	6.38 $^{+0.55}_{-6.38}$	0.32 $^{+1.14}_{-0.32}$	4.096 $^{+0.018}_{-0.020}$	0.160 $^{+0.075}_{-0.056}$
463.5337	0.64 $^{+0.07}_{-0.06}$	571 $^{+51}_{-29}$	10.78 $^{+0.49}_{-0.48}$	0.76	5.76 $^{+0.41}_{-5.76}$	1.50 $^{+0.22}_{-0.34}$	5.418 $^{+0.027}_{-0.027}$	1.930 $^{+0.212}_{-0.220}$
466.0262	0.62 $^{+0.07}_{-0.06}$	560 $^{+49}_{-55}$	9.94 $^{+0.55}_{-0.53}$	0.76	6.56 $^{+0.23}_{-0.32}$	0.69 $^{+0.41}_{-0.33}$	3.987 $^{+0.016}_{-0.022}$	0.485 $^{+0.123}_{-0.108}$
467.0082	0.95 $^{+5.14}_{-0.14}$	407 $^{+81}_{-407}$	12.68 $^{+0.32}_{-0.29}$	0.59	6.38 $^{+0.36}_{-0.67}$	0.25 $^{+0.80}_{-0.25}$	4.505 $^{+0.014}_{-0.014}$	0.169 $^{+0.065}_{-0.050}$
468.9646	0.59 $^{+0.18}_{-0.05}$	528 $^{+50}_{-152}$	8.88 $^{+0.53}_{-0.93}$	0.93	7.00 $^{+7.00}_{-0.36}$	1.75 $^{+1.75}_{-0.20}$	3.015 $^{+0.022}_{-0.018}$	0.537 $^{+0.083}_{-0.078}$
472.7545	0.87 $^{+0.12}_{-0.11}$	401 $^{+80}_{-77}$	10.04 $^{+0.34}_{-0.15}$	0.95	6.79 $^{+6.79}_{-0.24}$	0.45 $^{+0.37}_{-0.45}$	3.408 $^{+0.010}_{-0.011}$	0.270 $^{+0.047}_{-0.044}$
474.4141	0.78 $^{+0.10}_{-0.07}$	440 $^{+50}_{-80}$	11.05 $^{+0.21}_{-0.19}$	0.98	6.06 $^{+0.36}_{-6.06}$	1.33 $^{+0.36}_{-0.31}$	3.452 $^{+0.005}_{-0.010}$	0.847 $^{+0.076}_{-0.073}$

^a Unabsorbed flux of the EQPAIR model in units of 10^{-9} erg s $^{-1}$ cm $^{-2}$.

^b Unabsorbed flux of the Gaussian component in units of 10^{-12} erg s $^{-1}$ cm $^{-2}$.

^c Errors bars could not be constrained either due to low flux levels or degeneracies between model parameters.

Table 3. Same as Table 1 but for 2011 outburst.

JD-55000 (days)	t_h/t_s	kT_{bb} (eV)	τ_p	$\chi^2/\text{d.o.f.}$	Line Energy (keV)	Line Width (keV)	Flux $^a_{eqpair}$	Flux $^b_{gauss}$
849.3771	3.38 ^{+0.18} _{-0.16}	706 ⁺³² ₋₃₄	0.91 ^{+0.06} _{-0.06}	0.79	5.81 ^{+0.30} _{-5.81}	1.46 ^c _{-0.30}	0.779 ^{+0.007} _{-0.007}	0.225 ^{+0.026} _{-0.025}
851.0042	2.93 ^{+0.09} _{-0.08}	816 ⁺⁴⁷ ₋₃₉	1.67 ^{+0.15} _{-0.13}	0.62	6.38 ^{+0.20} _{-0.20}	0.82 ^{+0.25} _{-0.23}	2.366 ^{+0.013} _{-0.011}	0.320 ^{+0.049} _{-0.046}
852.4341	2.95 ^{+0.10} _{-0.14}	754 ⁺⁴⁷ ₋₆₅	1.40 ^{+0.15} _{-0.10}	0.56	6.40 ^{+0.20} _{-0.22}	0.62 ^{+0.29} _{-0.26}	1.527 ^{+0.010} _{-0.011}	0.164 ^{+0.036} _{-0.034}
855.5781	0.61 ^{+0.05} _{-0.04}	628 ⁺³⁸ ₋₃₉	10.89 ^{+0.33} _{-0.35}	0.66	6.04 ^{+0.18} _{-0.23}	1.21 ^{+0.18} _{-0.17}	13.256 ^{+0.059} _{-0.058}	5.105 ^{+0.477} _{-0.457}
858.1831	0.60 ^{+0.04} _{-0.04}	608 ⁺³³ ₋₃₈	10.22 ^{+0.33} _{-0.31}	0.43	6.24 ^{+0.18} _{-0.21}	1.00 ^{+0.19} _{-0.17}	12.033 ^{+0.054} _{-0.054}	3.419 ^{+0.394} _{-0.371}
859.6397	1.58 ^{+0.04} _{-0.05}	835 ⁺²² ₋₂₄	5.78 ^{+0.32} _{-0.22}	0.67	6.22 ^{+0.18} _{-0.20}	1.08 ^{+0.22} _{-0.19}	6.099 ^{+0.023} _{-0.024}	1.123 ^{+0.131} _{-0.126}
861.2436	0.83 ^{+0.10} _{-0.07}	586 ⁺⁴⁹ ₋₆₄	11.94 ^{+0.37} _{-0.32}	0.67	6.12 ^{+0.26} _{-0.30}	1.09 ^{+0.26} _{-0.23}	17.118 ^{+0.071} _{-0.071}	3.932 ^{+0.574} _{-0.542}
862.5005	0.66 ^{+0.06} _{-0.05}	617 ⁺⁴¹ ₋₄₂	11.56 ^{+0.35} _{-0.37}	0.64	5.97 ^{+0.18} _{-0.20}	1.26 ^{+0.16} _{-0.15}	15.866 ^{+0.070} _{-0.070}	7.209 ^{+0.582} _{-0.562}
863.3370	0.68 ^{+0.06} _{-0.05}	624 ⁺⁴⁸ ₋₄₉	11.67 ^{+0.35} _{-0.35}	0.44	6.02 ^{+0.19} _{-0.19}	1.30 ^{+0.14} _{-0.14}	17.155 ^{+0.074} _{-0.074}	8.264 ^{+0.600} _{-0.600}
864.2519	0.62 ^{+0.05} _{-0.05}	626 ⁺⁴¹ ₋₄₀	11.00 ^{+0.35} _{-0.39}	0.56	6.09 ^{+0.17} _{-0.20}	1.19 ^{+0.16} _{-0.15}	14.981 ^{+0.068} _{-0.067}	6.448 ^{+0.539} _{-0.519}
865.4324	0.56 ^{+0.04} _{-0.04}	691 ⁺³⁶ ₋₃₀	10.64 ^{+0.37} _{-0.42}	0.49	6.21 ^{+0.17} _{-0.21}	1.19 ^{+0.16} _{-0.16}	16.361 ^{+0.074} _{-0.072}	6.067 ^{+0.562} _{-0.536}
866.2953	0.66 ^{+0.06} _{-0.05}	655 ⁺⁴¹ ₋₄₃	11.77 ^{+0.38} _{-0.41}	0.41	5.88 ^{+0.20} _{-0.23}	1.40 ^{+0.17} _{-0.16}	17.792 ^{+0.077} _{-0.077}	8.830 ^{+0.668} _{-0.649}
867.2469	0.61 ^{+0.05} _{-0.05}	635 ⁺³⁹ ₋₃₉	11.04 ^{+0.36} _{-0.42}	0.75	6.07 ^{+0.21} _{-0.21}	1.24 ^{+0.16} _{-0.16}	15.794 ^{+0.071} _{-0.071}	7.012 ^{+0.580} _{-0.558}
867.9782	0.68 ^{+0.07} _{-0.06}	620 ⁺⁴² ₋₅₂	11.53 ^{+0.39} _{-0.44}	0.52	5.81 ^{+0.20} _{-5.81}	1.42 ^{+0.17} _{-0.16}	17.001 ^{+0.077} _{-0.077}	9.215 ^{+0.660} _{-0.643}
869.2827	0.63 ^{+0.05} _{-0.05}	616 ⁺⁴² ₋₄₀	11.07 ^{+0.34} _{-0.39}	0.41	6.08 ^{+0.18} _{-0.21}	1.19 ^{+0.15} _{-0.15}	13.766 ^{+0.065} _{-0.060}	5.515 ^{+0.490} _{-0.470}
871.2931	0.68 ^{+0.07} _{-0.06}	592 ⁺⁴⁷ ₋₅₀	11.39 ^{+0.37} _{-0.40}	0.53	5.77 ^{+0.18} _{-5.77}	1.41 ^{+0.15} _{-0.14}	15.326 ^{+0.070} _{-0.070}	9.212 ^{+0.602} _{-0.586}
872.0839	0.57 ^{+0.03} _{-0.04}	712 ⁺³⁹ ₋₂₆	10.92 ^{+0.36} _{-0.45}	0.62	6.35 ^{+0.18} _{-0.21}	1.09 ^{+0.19} _{-0.17}	16.554 ^{+0.070} _{-0.072}	5.194 ^{+0.545} _{-0.515}
873.0034	0.94 ^{+0.37} _{-0.10}	516 ⁺⁶¹ ₋₁₁₅	12.55 ^{+0.44} _{-0.27}	0.74	5.79 ^{+0.22} _{-5.79}	1.28 ^{+0.18} _{-0.17}	17.867 ^{+0.079} _{-0.066}	6.780 ^{+0.642} _{-0.623}
875.6732	0.58 ^{+0.05} _{-0.04}	684 ⁺³² ₋₄₁	11.00 ^{+0.40} _{-0.49}	0.62	6.31 ^{+0.20} _{-0.24}	1.17 ^{+0.21} _{-0.19}	15.484 ^{+0.068} _{-0.067}	5.087 ^{+0.532} _{-0.504}
876.8402	0.89 ^{+0.03} _{-0.03}	548 ⁺³⁶ ₋₆₆	12.72 ^{+0.25} _{-0.25}	0.57	6.13 ^{+0.21} _{-0.24}	1.20 ^{+0.20} _{-0.18}	16.308 ^{+0.067} _{-0.066}	5.238 ^{+0.551} _{-0.528}
877.4295	0.56 ^{+0.04} _{-0.03}	689 ⁺³⁰ ₋₃₆	10.47 ^{+0.33} _{-0.38}	0.56	6.33 ^{+0.18} _{-0.21}	1.07 ^{+0.19} _{-0.17}	14.428 ^{+0.063} _{-0.062}	4.497 ^{+0.474} _{-0.448}
877.8880	0.74 ^{+0.08} _{-0.06}	572 ⁺⁴⁹ ₋₅₅	11.80 ^{+0.34} _{-0.35}	0.62	5.82 ^{+0.19} _{-5.82}	1.36 ^{+0.15} _{-0.15}	14.142 ^{+0.063} _{-0.062}	6.943 ^{+0.532} _{-0.517}
879.5833	0.64 ^{+0.06} _{-0.05}	601 ⁺⁴¹ ₋₅₀	11.10 ^{+0.37} _{-0.38}	0.56	5.86 ^{+0.22} _{-5.86}	1.37 ^{+0.20} _{-0.18}	11.754 ^{+0.054} _{-0.054}	5.345 ^{+0.451} _{-0.436}
880.6295	0.61 ^{+0.05} _{-0.05}	631 ⁺⁴¹ ₋₄₁	10.97 ^{+0.37} _{-0.40}	0.73	6.19 ^{+0.18} _{-0.21}	1.18 ^{+0.17} _{-0.16}	12.253 ^{+0.054} _{-0.055}	4.687 ^{+0.430} _{-0.410}
882.6413	0.71 ^{+0.09} _{-0.06}	580 ⁺⁴⁹ ₋₆₂	11.71 ^{+0.41} _{-0.42}	0.59	5.89 ^{+0.20} _{-0.23}	1.28 ^{+0.18} _{-0.17}	12.552 ^{+0.057} _{-0.057}	5.804 ^{+0.478} _{-0.462}
883.5596	0.68 ^{+0.06} _{-0.06}	607 ⁺⁴¹ ₋₄₉	11.41 ^{+0.37} _{-0.38}	0.61	6.14 ^{+0.20} _{-0.24}	1.16 ^{+0.19} _{-0.19}	12.691 ^{+0.054} _{-0.057}	4.229 ^{+0.443} _{-0.422}
884.6704	0.63 ^{+0.05} _{-0.05}	591 ⁺⁴³ ₋₄₆	10.71 ^{+0.33} _{-0.37}	0.87	6.20 ^{+0.19} _{-0.22}	1.08 ^{+0.19} _{-0.17}	9.544 ^{+0.043} _{-0.044}	3.094 ^{+0.328} _{-0.311}
885.8371	0.62 ^{+0.04} _{-0.04}	607 ⁺³² ₋₃₂	10.52 ^{+0.34} _{-0.34}	0.60	6.28 ^{+0.18} _{-0.22}	1.08 ^{+0.20} _{-0.18}	9.571 ^{+0.041} _{-0.041}	2.921 ^{+0.317} _{-0.299}
886.8228	0.80 ^{+0.11} _{-0.07}	554 ⁺⁷² ₋₇₂	12.03 ^{+0.51} _{-0.51}	0.72	6.23 ^{+0.22} _{-0.26}	0.99 ^{+0.23} _{-0.22}	11.192 ^{+0.046} _{-0.048}	2.536 ^{+0.360} _{-0.338}
888.2533	0.60 ^{+0.04} _{-0.04}	586 ⁺³⁷ ₋₃₇	9.93 ^{+0.30} _{-0.38}	0.52	6.30 ^{+0.19} _{-0.23}	1.04 ^{+0.19} _{-0.17}	8.085 ^{+0.037} _{-0.038}	2.324 ^{+0.264} _{-0.249}
890.0729	0.59 ^{+0.05} _{-0.04}	605 ⁺³⁶ ₋₃₉	9.82 ^{+0.36} _{-0.36}	0.61	6.43 ^{+0.19} _{-0.23}	0.96 ^{+0.22} _{-0.20}	7.560 ^{+0.035} _{-0.035}	1.874 ^{+0.238} _{-0.222}
891.1884	0.62 ^{+0.05} _{-0.04}	596 ⁺³⁷ ₋₃₇	10.43 ^{+0.37} _{-0.35}	0.75	6.16 ^{+0.20} _{-0.24}	1.21 ^{+0.20} _{-0.18}	7.825 ^{+0.035} _{-0.035}	2.782 ^{+0.276} _{-0.262}
892.2633	0.67 ^{+0.07} _{-0.05}	566 ⁺⁴⁸ ₋₅₉	10.94 ^{+0.37} _{-0.39}	0.39	5.80 ^{+0.24} _{-5.80}	1.45 ^{+0.18} _{-0.18}	7.619 ^{+0.035} _{-0.036}	3.777 ^{+0.300} _{-0.290}
893.4686	0.67 ^{+0.08} _{-0.06}	570 ⁺⁵¹ ₋₅₈	11.29 ^{+0.40} _{-0.43}	0.69	6.06 ^{+0.27} _{-0.32}	1.16 ^{+0.26} _{-0.23}	7.265 ^{+0.034} _{-0.034}	1.971 ^{+0.264} _{-0.249}
894.3870	0.62 ^{+0.05} _{-0.05}	542 ⁺⁴⁸ ₋₄₈	9.72 ^{+0.34} _{-0.35}	0.59	6.34 ^{+0.23} _{-0.30}	0.99 ^{+0.26} _{-0.23}	5.417 ^{+0.026} _{-0.026}	1.141 ^{+0.175} _{-0.161}
895.2340	0.58 ^{+0.04} _{-0.04}	590 ⁺³⁷ ₋₃₇	9.68 ^{+0.36} _{-0.36}	0.60	6.38 ^{+0.25} _{-0.32}	1.06 ^{+0.27} _{-0.24}	5.619 ^{+0.026} _{-0.026}	1.233 ^{+0.184} _{-0.170}
896.1426	0.82 ^{+0.23} _{-0.10}	487 ⁺⁷⁰ ₋₁₂₇	12.02 ^{+0.37} _{-0.21}	0.69	6.43 ^{+0.25} _{-0.34}	0.73 ^{+0.36} _{-0.30}	5.939 ^{+0.027} _{-0.027}	0.699 ^{+0.174} _{-0.153}
898.1645	2.30 ^{+0.28} _{-1.57}	1 ⁺³⁹⁴ ₋₁	9.50 ^{+0.15} _{-0.14}	0.92	6.73 ^{+0.21} _{-0.25}	0.70 ^{+0.30} _{-0.26}	3.318 ^{+0.010} _{-0.010}	0.389 ^{+0.050} _{-0.046}
899.0077	0.74 ^{+0.19} _{-0.13}	444 ⁺¹⁰⁰ ₋₁₃₇	9.92 ^{+0.38} _{-0.78}	1.09	6.51 ^{+0.23} _{-0.25}	0.84 ^{+0.34} _{-0.25}	3.561 ^{+0.019} _{-0.019}	0.580 ^{+0.111} _{-0.099}
901.2278	2.90 ^{+0.17} _{-2.15}	1 ⁺⁴¹⁶ ₋₁	10.14 ^{+0.17} _{-0.11}	0.66	6.10 ^{+0.30} _{-0.41}	1.34 ^{+0.32} _{-0.26}	2.852 ^{+0.007} _{-0.006}	0.953 ^{+0.066} _{-0.064}
902.0756	0.79 ^{+1.67} _{-0.12}	407 ⁺⁹⁰ ₋₄₀₇	10.57 ^{+0.42} _{-0.52}	0.65	6.54 ^{+0.23} _{-0.31}	0.89 ^{+0.32} _{-0.13}	2.408 ^{+0.013} _{-0.013}	0.453 ^{+0.080} _{-0.073}
903.1209	2.24 ^{+0.77} _{-1.35}	23 ⁺³²⁰ ₋₂₃	10.88 ^{+0.24} _{-0.22}	0.76	6.77 ^{+0.20} _{-0.23}	0.77 ^{+0.31} _{-0.26}	1.550 ^{+0.005} _{-0.005}	0.254 ^{+0.028} _{-0.027}
904.0978	0.99 ^{+0.25} _{-0.23}	199 ⁺¹⁹⁴ ₋₁₉₉	7.77 ^{+0.11} _{-0.10}	1.08	6.03 ^{+0.24} _{-0.32}	1.42 ^{+0.26} _{-0.21}	1.037 ^{+0.004} _{-0.004}	0.644 ^{+0.029} _{-0.029}
889.1765	0.98 ^{+0.14} _{-0.14}	443 ⁺⁸⁵ ₋₄₄₃	12.50 ^{+0.35} _{-0.36}	0.78	5.83 ^{+0.26} _{-5.83}	1.12 ^{+0.23} _{-0.20}	9.245 ^{+0.042} _{-0.040}	2.139 ^{+0.329} _{-0.312}
900.3845	1.26 ^{+1.50} _{-0.54}	142 ⁺³⁰² ₋₁₄₂	10.08 ^{+0.29} _{-0.29}	1.00	6.15 ^{+0.33} _{-0.44}	1.47 ^{+0.00} _{-0.27}	2.751 ^{+0.015} _{-0.015}	0.722 ^{+0.108} _{-0.100}
905.3416	0.57 ^{+0.05} _{-0.05}	291 ⁺³⁰ ₋₃₇	0.40 ^{+0.07} _{-0.06}	0.62	5.60 ^{+0.18} _{-5.60}	1.61 ^{+0.09} _{-0.14}	0.778 ^{+0.006} _{-0.005}	0.523 ^{+0.027} _{-0.030}
906.0508	1.57 ^{+0.07} _{-0.07}	672 ⁺⁷⁰ ₋₁₆₂	1.44 ^{+0.58} _{-0.18}	1.00	5.60 ^{+0.15} _{-5.60}	1.22 ^{+0.19} _{-0.19}	0.686 ^{+0.002} _{-0.012}	0.182 ^{+0.024} _{-0.024}
907.3148	2.67 ^{+0.14} _{-0.14}	684 ⁺²⁸ ₋₂₈	0.71 ^{+0.04} _{-0.04}	0.80	5.65 ^{+0.15} _{-5.65}	1.39 ^{+0.18} _{-0.14}	0.476 ^{+0.004} _{-0.004}	0.228 ^{+0.015} _{-0.015}
908.2906	2.72 ^{+0.09} _{-0.26}	823 ⁺²⁹ ₋₅₉	0.91 ^{+0.09} _{-0.04}	3.48	5.60 ^c	0.51 ^c	0.358 ^{+0.002} _{-0.006}	0.000 ^{+0.000} _{-0.000}
909.0731	2.67 ^{+0.19} _{-0.31}	697 ⁺⁵⁶ ₋₆₈	0.97 ^{+0.12} _{-0.04}	1.66	6.79 ^c	0.25 ^{+1.26} _{-0.25}	0.253 ^{+0.003} _{-0.005}	0.006 ^{+0.005} _{-0.005}
910.2218	3.58 ^{+1.18} _{-0.87}	668 ⁺¹¹¹ ₋₁₁₅	0.84 ^{+0.24} _{-0.22}	0.69	6.41 ^{+0.38} _{-0.38}	0.25 ^{+1.20} _{-0.25}	0.115 ^{+0.006} _{-0.005}	0.011 ^{+0.006} _{-0.006}
904.1780	1.66 ^c	1 ⁺³⁸⁷ ₋₁	7.52 ^{+0.11} _{-0.11}	0.83	5.73 ^{+0.17} _{-0.17}	1.74 ^{+0.11} _{-0.11}	1.011 ^{+0.005} _{-0.006}	0.911 ^{+0.039} _{-0.045}
904.3096	0.80 ^{+0.79} _{-0.10}	334 ⁺⁹⁸ ₋₃₂₇	7.76 ^{+0.14} _{-0.15}	0.75	5.74 ^{+0.17} _{-0.10}	1.75 ^{+0.11} _{-0.11}	0.988 ^{+0.005} _{-0.006}	0.863 ^{+0.036} _{-0.042}
906.3936	1.92 ^{+0.07} _{-0.08}	736 ⁺⁹¹ ₋₂₃₁	1.30 ^{+0.32} _{-0.36}	1.26	5.60 ^{+0.21} _{-5.60}	1.15 ^{+0.22} _{-0.21}	0.640 ^{+0.002} _{-0.013}	0.154 ^{+0.026} _{-0.026}
908.0061	2.27 ^{+0.23} _{-0.18}	778 ⁺⁶⁸ ₋₁₂₁	1.15 ^{+0.26} _{-0.13}	1.60	5.60 ^c	1.21 ^c	0.399 ^{+0.007} _{-0.007}	0.000 ^{+0.000} _{-0.000}
909.2486	2.63 ^{+0.31} _{-0.23}	683 ⁺⁸² ₋₉₉	1.06 ^{+0.14} _{-0.14}	1.56	6.02 ^c	0.25 ^c	0.238 ^{+0.005} _{-0.004}	0.000 ^{+0.000} _{-0.000}